Increasing the energy dynamic range of solid-state nuclear track detectors using multiple surfaces

A. B. Zylstra,[a] H. G. Rinderknecht, N. Sinenian, M. J. Rosenberg, M. Manuel, F. H. Séguin, D. T. Casey, J. A. Frenje, C. K. Li, and R. D. Petrasso
Plasma Science and Fusion Center, Massachusetts Institute of Technology, Cambridge, Massachusetts 02139, USA

(Received 15 March 2011; accepted 10 July 2011; published online 10 August 2011)

Solid-state nuclear track detectors, such as CR-39, are widely used in physics and in many inertial confinement fusion (ICF) experiments. In the ICF experiments, the particles of interest, such as D^3He-protons, have ranges of order of the detector thickness. In this case, the dynamic range of the detector can be extended by recording data on both the front and back sides of the detector. Higher energy particles which are undetectable on the front surface can then be measured on the back of the detector. Studies of track formation under the conditions on the front and back of the detector reveal significant differences. Distinct front and back energy calibrations of CR-39 are therefore necessary and are presented for protons. Utilizing multiple surfaces with additional calibrations can extend the range of detectable energies on a single piece of CR-39 by up to 7-8 MeV. The track formation process is explored with a Monte Carlo code, which shows that the track formation difference between front and back is due to the non-uniform ion energy deposition in matter. © *2011 American Institute of Physics*. [doi:10.1063/1.3617475]

I. INTRODUCTION

Solid-state nuclear track detectors (SSNTDs) were developed in the beginning of the 1950s with LiF (Ref. 1) and mica.[2] When a high energy charged particle is incident upon the solid dielectric detector it ionizes the matter along its path. The damaged region corresponding to the particle trajectory is chemically altered due to the ionization. If the detector is then exposed to a chemical etchant such that the etch rate for the damaged material is greater than for the undamaged material, a physical "pit" or "track" is created. These tracks can then be observed with an optical microscope. SSNTDs are in widespread use today.

In inertial confinement fusion (ICF) experiments, CR-39 was used in the first direct measurement of fuel ρR.[3] More recently, diagnostics based on SSNTDs, such as CR-39, have been used to measure absolute spectra of various fusion products,[4–6] from which ρR, yield, and T_i (Ref. 7) of an implosion can be determined.

Recent techniques in imaging ICF implosions using proton backlighter radiography[8] in fast-ignition relevant[9] and indirect-drive[10] configurations have led to important physics results. Proposed future experiments include direct-drive radiography and warm/hot matter stopping power experiments. In these studies of electromagnetic fields in ICF implosions it is necessary to spatially resolve the imaging particle energies across the detector. For this, the detector response as a function of energy must be characterized. This has been carefully studied for a particle incident on the front surface of a CR-39 SSNTD.[4,11]

In the proton radiography experiments a detector pack consisting of two pieces of CR-39 is assembled as shown in Fig. 1. A thin Ta filter (generally $\geq 5\mu$m) is placed in front to range out fast ablator ions produced in laser-plasma interactions.[12] The Al filter between the two CR-39 detectors is usually chosen to optimize the high-energy proton (from $D+^3He$) detection on the second piece of CR-39. This allows simultaneous imaging of both high and low energy particles from the fusion reactions

$$D + {}^3He \rightarrow {}^4He(3.6MeV) + p(14.7MeV), \quad (1)$$

$$D + D \rightarrow T(1.01MeV) + p(3.02MeV). \quad (2)$$

Additional reactions generally relevant to ICF are the second branch DD reaction ($D + D \rightarrow n + {}^3He$) and the DT reaction ($D + T \rightarrow n + {}^4He$) but none of these products has been used in the radiography experiments so far. These backlighting particles are generated in a thin-glass shell (low ρR) implosion in a short (~80 ps duration) shock coalescence burn.[8] In principle, all four fusion products from Eqs. (1) and (2) can be used for radiography; in practice the 3 and 14.7 MeV protons are the most useful.[8,10,13] Proof-of-principle simultaneous detection of p, T, ^{3}He, and ^{4}He, from DD and D^3He fusion on an accelerator fusion product source is shown in Fig. 2.

The response of CR-39 to energetic charged particles has been extensively studied experimentally[4,11,14–24] and theoretically[25] for particles incident on the front surface of the detector. In this work, as well as several of the cited works, TasTrak®CR-39 was used. Since the highest energy protons traverse the entire first detector an image will also be generated on the back surface of the first detector, if the energy loss is enough that the proton energy at the back surface is in the detectable range (0-8 MeV). These protons generally lose 8-11 MeV through the first CR-39 detector in the proton radiography experiments. The energy characteristics of the detector response on the back surface are found to be significantly different from the previously-measured front surface.

[a]Electronic mail: zylstra@mit.edu.

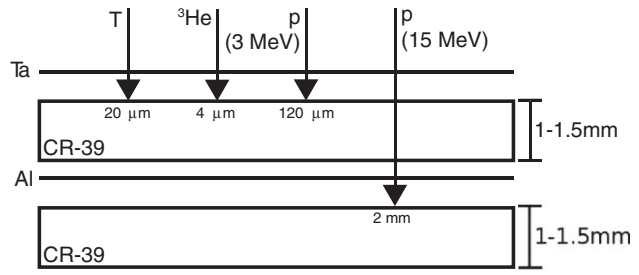

FIG. 1. SSNTD configuration for proton radiography using fusion products (Eqs. (1) and (2)). The maximum range (i.e., with 0 μm of Ta filtering in front) of each particle in CR-39 is shown. The low energy particles (T, ^{4}He, and 3 MeV p) are recorded on the first CR-39 detector. The 14.7 MeV p are too energetic to be seen on the front of the first detector since the track size $\sim dE/dx$. However, they are recorded both on the back surface of the first detector and the front surface of the second detector.

To accurately infer an energy of the incident particles from this data, the detector energy response must be characterized for charged particles traversing the entire SSNTD, which is the focus of this work.

The paper is structured as follows. Section II gives a simple model for track formation in SSNTDs. Section III describes the experimental setup used to characterize the detector energy response. Section IV shows and discusses the experimental results. Section V presents a simple Monte Carlo simulation of the track formation process, which is interpreted in Sec. VI. Finally, the paper is concluded in Sec. VII.

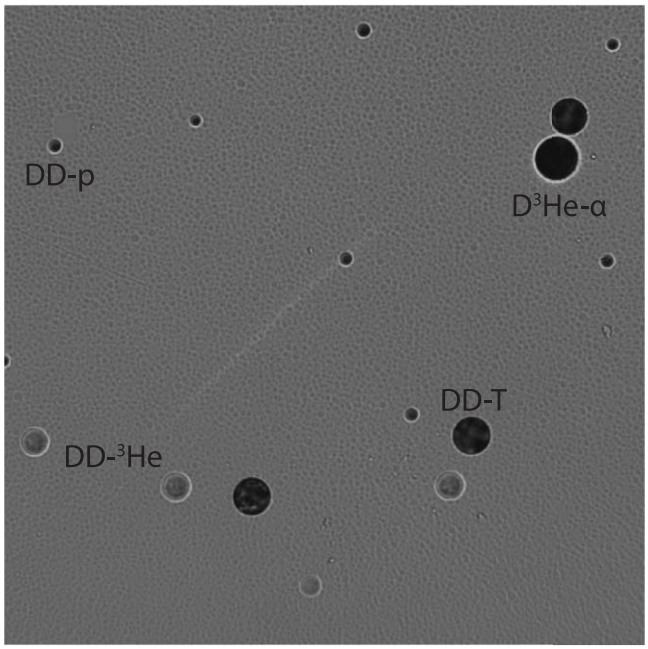

FIG. 2. Four types of particle track in CR-39 after a 3 h etch. Shown are DD-p (D $\approx 4\mu$m), DD-^{3}He (D $\approx 9\mu$m), DD-T (D $\approx 13\mu$m), and D^{3}He-^{4}He (D $\approx 14\mu$m). For DD-p, DD-T, and D^{3}He-^{4}He the track contrast is $\geq 90\%$ as defined in this work; the DD-^{3}He have contrast $60\% - 70\%$ (see Appendix B). The 14.7 MeV D^{3}He protons are undetectable in this scheme, since they are not ranged down into the detectable energy range. The CR-39 was filtered with only 1μm of aluminized mylar to allow detection of the ^{3}He ions. The image size is 208μm square.

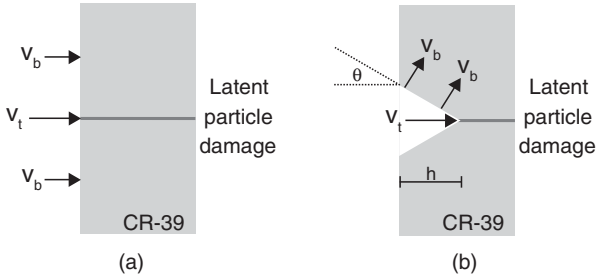

FIG. 3. An overview of the track etching process in SSNTDs. (a) SSNTD at the start of the etch process. The latent particle damage is unobservable with conventional techniques ($\sim$5 nm in size). (b) After some etch time a track is developed. Typical track diameters are $2-30\mu$m depending on particle species, energy, and etch time.

II. TRACK FORMATION

The theory of track formation in SSNTDs is well-developed.[26,27] In the idealized case the particle's energy deposition in the bulk material creates a region in which the chemical composition of the material is altered. This results in different chemical etch rates of the undamaged and damaged material: the bulk (v_b) and track (v_t) etch rates.

A detector schematic before and after the etch process is shown in Figs. 3(a) and 3(b), respectively. In typical SSNTDs $v_t > v_b$ which results in a conical track defined by the track depth h and angle θ. In particular, we can write that

$$\sin\theta = \frac{v_b}{v_t}. \tag{3}$$

In the case of normal particle incidence and constant track etch rate, the track depth is

$$h = (v_t - v_b)\tau, \tag{4}$$

for some etch duration τ. Then we can write that the track diameter is

$$D = 2h\tan\theta = 2h\sqrt{\frac{v_b^2}{v_t^2 - v_b^2}}. \tag{5}$$

The track etch rate v_t is a monotonically increasing function of the energy lost to low-energy electrons, which create the latent damage in the material. Higher-energy electrons do not locally deposit their energy and thus do not contribute to track formation. In the literature the energy loss rate to low-energy electrons (below some critical recoil energy) is referred to as the restricted energy loss rate, which then depends on dE/dx for the incident particle. We can thus see how the diameter of a track will corresponds to its energy, based on Eq. (5).

Typically the bulk etch rate is $2-3$ μm/h, the track etch rate is $4-6$ μm/h, giving a typical ratio in Eq. (3) as 1/2 and a typical track depth of $2-3$ μm/h by Eq. (4). The range of detectable track diameters is typically $2-30$ μm depending on the particle type and energy. These typical numbers can vary between CR-39 manufacturing batches.

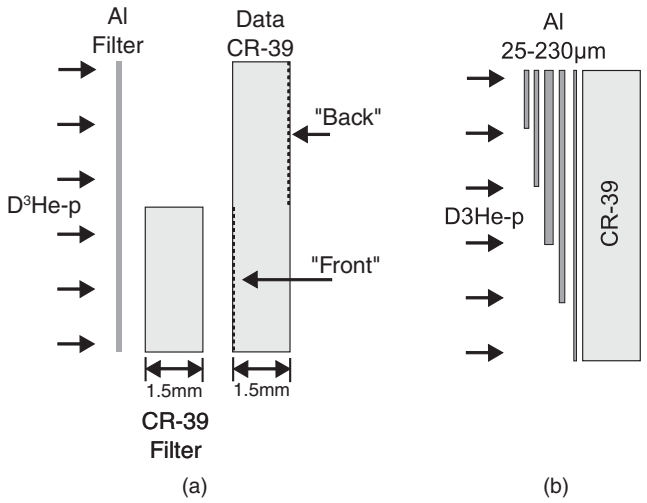

FIG. 4. Filtering configuration for the accelerator fusion product source experiments. (a) Filters for equivalent known energy distributions at the front and back surface of a single detector using both Al and a CR-39 filter. (b) Several energy windows are created through different Al thicknesses. (a) and (b) are orthogonal depictions of the filter pack. For a given Al thickness, a CR-39 filter is used to create identical energy distributions at the front and back surface of the data CR-39 (a). In an orthogonal direction, multiple Al thicknesses are used to vary the energy distribution over five windows (b).

III. EXPERIMENTAL OVERVIEW

Experimental studies of the properties of CR-39 SSNTDs have been conducted using an accelerator-based fusion products source.[28] In these experiments, we use a 140 kV linear electrostatic accelerator. Either D or ^{3}He beams were incident on a ErD_2 target. These targets were additionally doped with ^{3}He. Therefore, we were able to produce the fusion products in Eqs. (1) and (2) with typical reaction rates of order 10^6 and 10^5 s^{-1} for DD and D^{3}He, respectively, using a D beam.

In these experiments, CR-39 detectors were exposed to D^{3}He protons with different energies, depending on the filtering in front of the CR-39 (see Fig. 4). These proton spectra were measured with a silicon surface barrier detector, which had been calibrated with a ^{226}Ra alpha source to an accuracy of $\pm$75 keV.

The filter configuration shown schematically in Fig. 4 is used to range D^{3}He protons to 2.5$-$6.5 MeV. Images of the filter pack are shown in Fig. 5. Equivalent energy distributions are created on the front and back surfaces of the CR-39 through the use of a CR-39 filter,[29] as shown in Fig. 4(a). This allows investigation of fundamental differences in the detector behavior for protons at the front and back surface. Several discrete energy windows are created by varying the aluminum filter in front of the detector (Fig. 4(b)). Thus, a single piece of CR-39 is exposed to five distinct proton energy distributions on both the front and back surfaces.

After exposure, the CR-39 SSNTDs were etched in a six molar NaOH solution for 2$-$6 h. Digital microscope systems with automatic track image recognition algorithms are used to identify the diameter, eccentricity, and contrast of each track on the detector.

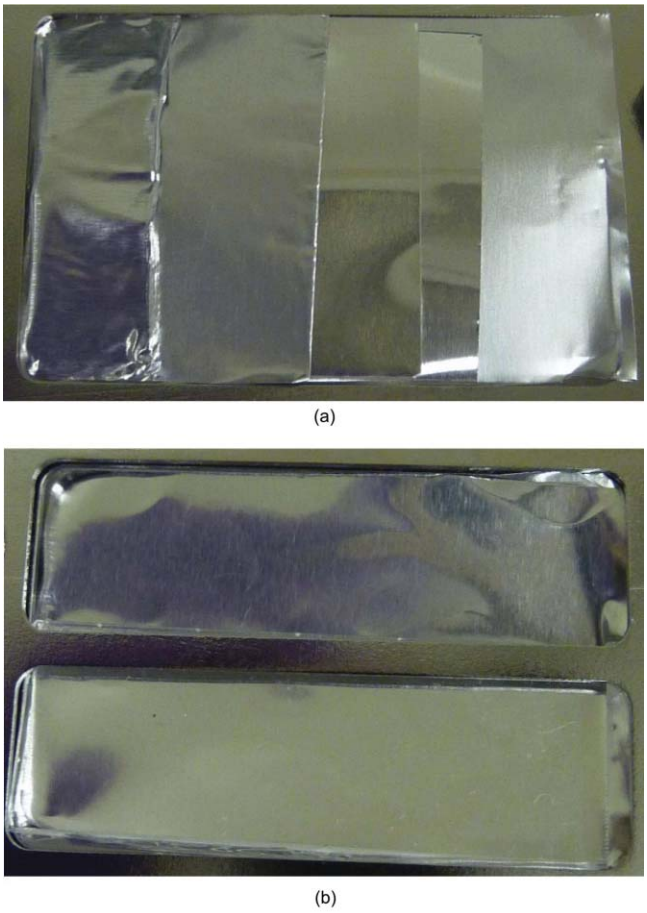

FIG. 5. (Color online) Images of the filter pack used in this experiment. (a) Front view (looking along proton trajectory) of filter pack. Five energy windows are created via varying the aluminum thickness, which increases from right to left. (b) Back view (looking towards proton source) of filter pack. The CR-39 filter is visible in the bottom half.

IV. RESULTS

Sample diameter distributions are plotted for several energies in Fig 6. Figure 6(a) shows the resulting track diameter distributions detected on the front surface of the CR-39, while Fig. 6(b) shows the diameter distributions for the back surface. In the lowest energy window, we can clearly see that the back surface diameter distributions have larger means and standard deviations than on the front. Additionally, the lowest energy spectrum on the back surface displays a sharp cutoff at $D \approx 22\mu$m.

In Fig. 7, the mean diameter versus proton energy is illustrated for 2, 4, and 6 h etch times for the front (solid line) and back (dashed line) surfaces. The back surface systematically shows larger diameters for all etch times at low energies. The front vs back surface discrepancy is larger for lower energies and the two D vs E trends converge at high energies ($\approx$6 MeV). The highest energy window ($\sim$6.5 MeV) was not detectable at the 2 h etch time.

Contour plots of the number of tracks observed versus diameter and contrast, which is defined as the minimum light transmission through the track normalized to the background level during the optical scan, are plotted in Fig. 8 for the front surface (a) and back surface (b). A perfectly dark track

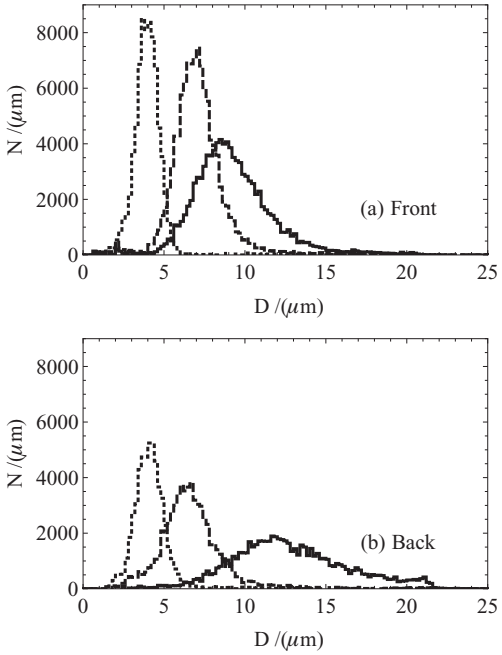

FIG. 6. Sample track diameter spectra on a single CR-39 detector for the front (a) and back (b) sides of the CR-39 SSNTD after 6 h etching time. The incident energy distributions observed are identical in each case (see Fig. 4) with mean energies of 2.55 MeV (solid line), 4.14 MeV (dashed line), and 5.68 MeV (dotted line). Contrast plots for the 2.55 MeV data are shown in Fig. 8.

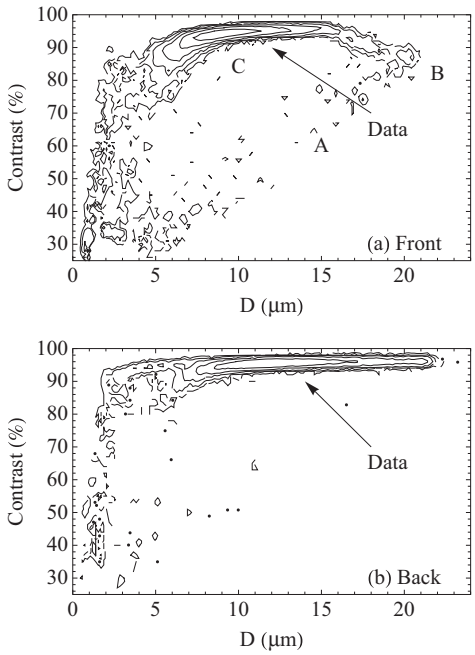

FIG. 8. Contour plots of the number of tracks versus track contrast and diameter for the same piece of CR-39 in Fig. 6. Data for 2.55 MeV protons are shown for the front side (top, with regions of data identified with stopping power regimes) and the back side (bottom). Intrinsic CR-39 noise appears in the low-contrast low-diameter regime. Contours represent a constant number of tracks per unit contrast and diameter; the values of this quantity corresponding to plotted contours form a geometric series with a ratio of 3. As defined in this work a high contrast number is a dark track, while a low contrast number is a light track (see Fig. 2).

corresponds to 100% contrast and a very faint track would have low contrast. For an example of how this contrast definition compares to microscope images see Fig. 2, which shows both high- and low- contrast particle tracks, and Appendix B which shows the resulting contrast contour plot. At small diameters and low contrast intrinsic noise (defects in the CR-39) is observed. This intrinsic noise is eliminated in a normal analysis through contrast and diameter limits. The contrast contour plots show a clear qualitative difference in behavior between the data on the front and back surfaces. On the front surface, we see the data region curves to lower contrast (as defined) for the extreme diameters. On the back surface contrast plot, we observe that the data contrast is independent of track diameter.

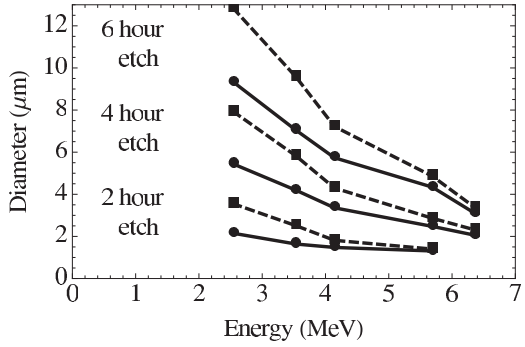

FIG. 7. Diameter of tracks observed versus energy for 2, 4, and 6 h etch time. Solid lines represent the front CR-39 surface, dashed lines represent the back surface. Example distributions are shown in Fig. 6.

The stopping power for a proton in the detector is calculated with SRIM software[30] and plotted in Figure 9. The proton Bragg peak in the CR-39 is observed at around 100 keV. For most of the detected protons, since the distribution mean is of order MeV, we are dealing exclusively with average ion energies higher than the Bragg peak. Therefore, as a proton traverses the detector, its energy decreases and dE/dx increases for the front surface (see Fig. 9). Since the amount of damage done to the CR-39 increases monotonically with the increasing stopping power, we can say that the size of the latent damage track created by the particle will be increasing

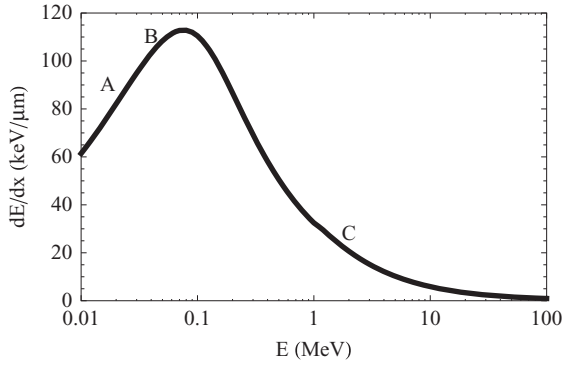

FIG. 9. Stopping power for protons in CR-39, given as change in energy per unit length. Protons of order of MeV (**C**) create small dark tracks. Around the Bragg peak (**B**) protons create large tracks due to the large dE/dx. For protons that stop in the etched plastic (**A**) the track etches away and becomes light and hard to detect. These features are labeled in Fig. 8(a).

along the direction of the particle trajectory. This is annotated in Figs. 9 and 8(a) by the label **C**.

Since the distribution functions in this experiment are so broad (see Fig. 6 and Appendix A) there is a low-energy tail which also samples energies near the Bragg peak. Protons near the Bragg peak create very large tracks due to the high stopping power (annotated in Figs. 9 and 8(a) by the label **B**). But if the proton stops within the CR-39 material removed during the etch (bulk material removed is $\sim 2\mu$m/h) then the track shape deviates significantly from conical once the etch proceeds past the end of the latent track. In this case the measured track contrast decreases (lighter tracks) and the diameter decreases, as annotated in Figs. 9 and 8(a) by the label **A**.

V. SIMULATED RESPONSE

To explore the CR-39 response to protons of various energies, a simple Monte Carlo track formation code was developed and used. Incident particles sampled from an arbitrary energy distribution are ranged in the detector material using SRIM-calculated stopping powers.[30] This defines the formation of the latent track. The etching process is then simulated for a given etch time using a model previously developed with nominal parameters for CR-39.[31] Transmission of a uniform backlight through the track using Fresnel's equations then simulates the automated microscope-based scanning process. Refraction in the conical track defines the observed diameter and contrast of a track.

The simulated results are shown in Fig. 10 for a uniform energy distribution from 0.1 to 10.0 MeV to sample the full range of track behavior. Many of the interesting features in the contrast-diameter space (such as labels **A** and **B** in Fig. 8(a)) come from the low-energy tail of the distribution, which is created by straggling and blooming effects in the filter. This is more difficult to model, so the uniform energy distribution is used to map out the trajectory of tracks as the energy is changed in the contrast-diameter space.

The simulated data on the detector front surface are shown in Fig. 10(a), and the simulated back surface data shown in Fig. 10(b). From these distributions, we can clearly see that the simulation qualitatively matches features of the data as shown in Fig. 8. The front surface data show a low-contrast tail at the maximum observed diameter which is not observed on the back surface. Additionally, the maximum diameter observed is larger on the back surface. Both of these effects are observed in the data.

Additionally, the simulation reproduces the effect that the back surface diameters are larger than the front, although the simulated effect is much smaller than the data indicates. Differences between the simulation and data are likely explained by the choice of the two free parameters in the track formation model.[31]

VI. INTERPRETATION

The only difference between the front and back surface simulation is the sign of $d/d\chi(dE/dx)$, where χ is the distance of the etch into the bulk detector material: dE/dx increases along the etch direction for data on the front surface whereas it decreases along the etch direction on the back surface. This indicates that the observed differences in the data for the front and back surfaces is due to energy deposition effects in the SSNTD, which is known to affect the resulting track shape.[26] The ratio of track to bulk etch rate, as discussed in Sec. II, defines the track cone angle. If the stopping power along the track length is constant then the cone angle is constant and the overall track shape is perfectly conical. However, when the stopping power (and thus track etch rate) changes

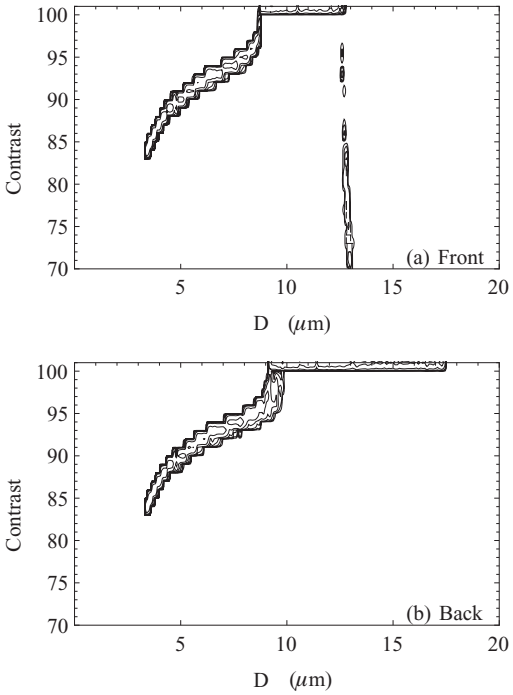

FIG. 10. Simulated contour plots of the number of tracks observed (arbitrary) versus track contrast and diameter. Plots are shown for the front (a) and back (b) surfaces. Contours represent a constant number of tracks per unit contrast and diameter; the values of this quantity corresponding to plotted contours form a geometric series with a ratio of 3.

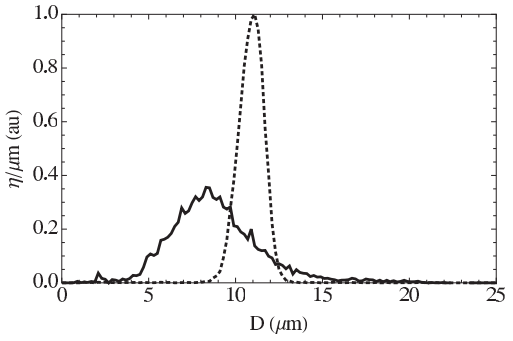

FIG. 11. Sample track diameter spectra on CR-39 detector for D^3He-p ranged down to 2.55 MeV (solid line) versus DD-p (see (2)) ranged down to 2.4 MeV (dotted line). The two distributions are area normalized and plotted in arbitrary units per μm. The observed distribution widths are $\sigma = 0.72\,\mu$m for the DD-p versus $\sigma = 2.69\mu$m for the D^3He-p. This is due to broadening of the initial spectrum due to dispersion, straggling, and blooming in the filtering for D^3He as the energy loss is approximately 12 MeV. Some of the discrepancy in the mean is due to piece-to-piece CR39 variation.

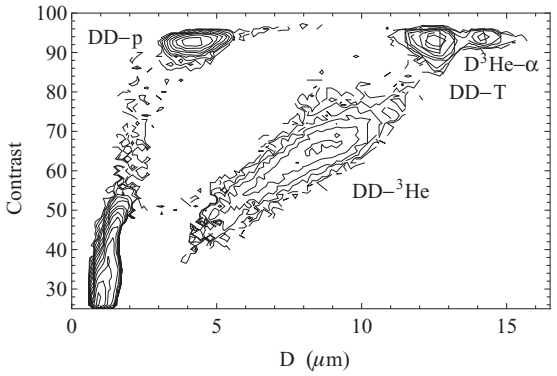

FIG. 12. Contour plots of the number of tracks versus track contrast and diameter for the same piece of CR-39 in Fig. 2. The four particle species visible are labeled on the plot, compare to the microscope image in Fig. 2. Intrinsic CR-39 noise appears in the low-contrast low-diameter regime. Contours represent a constant number of tracks per unit contrast and diameter; the values of this quantity corresponding to plotted contours form a geometric series with a ratio of 2. As defined in this work a high contrast number is a dark track, while a low contrast number is a light track.

as a function of distance along the track then the cone angle changes over the track. This causes curvature of the track surface, as discussed in detail by Henke and Benton.[26] We, therefore, interpret the difference in front vs back diameter versus particle energy (Fig. 7) as a result of the track formation process with $d/d\chi(dE/dx)$ positive (front) versus negative (back).

The other major feature is the different behavior at large diameters between the front and back (Fig. 8). In the front side data around the maximum proton diameter the contrast of data tracks (as defined) tends to decrease. This is a common feature of CR-39 data. The maximum proton diameter occurs for proton energies near the Bragg peak since the track size $\sim dE/dx$. However, the range of protons near the Bragg peak in CR-39 is about the same as the bulk material removed during the etching process ($\sim 2\ \mu$m/h). Therefore, these large-diameter proton tracks are etched beyond the end of the track, which increases the light transmission (leading to lower contrast or lighter tracks in Fig. 8) and decreases the observed diameter. The back side data also have the maximum proton diameter observed for tracks where the proton energy was near the Bragg peak, but in this case as the bulk material is etched away tracks do not disappear since the etch direction is opposite to the particle velocity. This causes the characteristic flat contrast shape at large diameters as observed in the data. In this case, the maximum proton diameter is also closer to the theoretical maximum ($2v_b \times \tau$) since tracks do not disappear or "etch away" during the etch process.

VII. CONCLUSIONS

Distinct energy calibrations have been measured on an accelerator-based fusion products source for both the front and back surfaces of CR-39, a solid-state nuclear track detector. We observe significant differences in track formation for identical energy distributions between the two surfaces, which result from a dependence of the final track shape on whether dE/dx increases or decreases along the track etch direction. This is verified by simulated data using a Monte Carlo track formation code. The observed effects illustrate that equivalent distributions create larger track diameters on the back, and that the back side tracks have consistent contrast while on the front side low energy proton tracks are etched away. This demonstrates the importance of separate front and back surface energy calibrations for CR-39 based proton diagnostics in ICF experiments, such as in proton radiography. Characterizing both detector surfaces thus extends, in a practical fashion, the range of detectable energies on a single piece of CR-39 by up to 7-8 MeV.

ACKNOWLEDGMENTS

The authors would like to thank J. Schaeffer and R. Frankel for contributing to the CR-39 processing for this work, and R. A. Childs for contributing to the continuing development of the electrostatic accelerator used in this study.

This work was supported in part by (U.S.) Department of Energy (DOE) (Grant No. DE-FG03-03SF22691), LLE (No.412160-001G), LLNL (No.B504974), and GA under DOE (DE-AC52-06NA27279). A. Zylstra is supported by the Stewardship Science Graduate Fellowship (DE-FC52-08NA28752).

APPENDIX A: DISTRIBUTION WIDTH

In this experiment many important effects are observed for protons near the Bragg peak (see Figs. 8–10). It is important to note that these observations are possible even though the mean energies of each proton distribution are all over several orders of MeV. This is because the diameter distributions, as shown in Figs. 6 and 11, have standard deviations up to $\sim 3\mu$m resulting from ranging down the protons from 14.7 MeV. In this experiment each energy window has $\sim 2 \times 10^4$ particles, so with a sufficiently broad distribution we can sample a wide range of track behavior. Thus, the low-energy tail of the energy distribution allows us to probe behavior close to the Bragg peak for proton distributions in the order of MeV.

APPENDIX B: TRACK CONSTRAST

The contrast contour plot for the four particle data in Fig. 2 is shown in Fig. 12. The fusion product energies are given in Eqs. (1) and (2). The protons, tritons, and alphas have ranges greater than the etch distance and, thus, have fully formed high-contrast (dark) tracks. When the cone angle is above a critical value then all light is reflected out, and in theory the track contrast is 100%. This is true for the protons, tritons, and alphas. The diameter of each species track is related to the stopping power as discussed in Sec. II. The DD-^{3}He particles have a shorter range than the bulk amount of material removed during the etch and thus the tracks are being "etched out", resulting in the significantly lower contrast.

TABLE I. Shot numbers for data shown in each figure.

Figure	Shot number
2	A2010083101
6	A2010021204
7	A2010021203-5
8	A2010021204
11	A2010021204
	A2010020101
12	A2010083101

APPENDIX C: SHOT NUMBERS

For reference purposes, facility shot numbers for all data given in this paper are tabulated in Table I.

[1]D. Young, Nature (London) **182**, 375 (1958).
[2]E. Silk and R. Barnes, Philos. Mag. **4**, 970 (1959).
[3]S. Kacenjar, S. Skupsky, A. Entenberg, L. Goldman, and M. Richardson, Phys. Rev. Lett. **49**, 463 (1982).
[4]F. Séguin, J. Frenje, C. Li, D. Hicks, S. Kurebayashi, J. Rygg, B. Schwartz, R. Petrasso, S. Roberts, J. Soures, D. Meyerhofer, T. Sangster, J. Knauer, C. Sorce, V. Glebov, C. Stoeckl, T. Phillips, R. Leeper, K. Fletcher, and S. Padalino, Rev. Sci. Instrum. **74**, 975 (2003).
[5]J. Frenje, K. Green, D. Hicks, C. Li, F. Séguin, R. Petrasso, T. Sangster, T. Phillips, V. Glebov, D. Meyerhofer, S. Roberts, J. Soures, C. Stoeckl, K. Fletcher, S. Padalino, and R. Leeper, Rev. Sci. Instrum. **72**, 854 (2001).
[6]J. Frenje, C. Li, F. Séguin, D. Hicks, S. Kurebayashi, R. Petrasso, S. Roberts, V. Glebov, D. Meyerhofer, T. Sangster, J. Soures, C. Stoeckl, C. Chiritescu, G. Schmid, and R. Lerche, Rev. Sci. Instrum. **73**, 2597 (2002).
[7]C. Li, D. Hicks, F. Séguin, J. Frenje, R. Petrasso, J. Soures, P. Radha, V. Glebov, C. Stoeckl, D. Harding, J. Knauer, R. Kremens, F. Marshall, D. Meyerhofer, S. Skupsky, S. Roberts, C. Sorce, T. Sangster, T. Phillips, M. Cable, and R. Leeper, Phys. Plasmas **7**, 2578 (2000).
[8]C. Li, F. Séguin, J. Frenje, J. Rygg, R. Petrasso, R. Town, P. Amendt, S. Hatchett, O. Landen, A. Mackinnon, P. Patel, V. Smalyuk, J. Knauer, T. Sangster, and C. Stoeckl, Rev. Sci. Instrum. **77**, 10E725 (2006).
[9]J. Rygg, F. Seguin, C. Li, J. Frenje, M. Manuel, R. Petrasso, R. Betti, J. Delettrez, O. Gotchev, J. Knauer, D. Meyerhofer, F. Marshall, C. Stoeckl, and W. Theobald, Science **319**, 1223 (2008).
[10]C. Li, F. Seguin, J. Frenje, M. Rosenberg, R. Petrasso, P. Amendt, J. Koch, O. Landen, H. Park, H. Robey, R. Town, A. Casner, F. Philippe, R. Betti, J. Knauer, D. Meyerhofer, C. Back, J. Kilkenny, and A. Nikroo, Science **327**, 1231 (2010a).
[11]N. Sinenian, M. Rosenberg, M. Manuel, S. McDuffee, D. Casey, A. Zylstra, H. Rinderknecht, M. Gatu Johnson, F. Séguin, J. Frenje, C. Li, and R. Petrasso, Rev. Sci. Instrum. (submitted).
[12]D. Hicks, C. Li, F. Séguin, J. Schnittman, A. Ram, J. Frenje, R. Petrasso, J. Soures, D. Meyerhofer, S. Roberts, C. Sorce, C. Stoeckl, T. Sangster, and T. Phillips, Phys. Plasmas **8**, 606 (2001).
[13]C. Li, F. Séguin, J. Frenje, M. Rosenberg, A. Zylstra, R. Petrasso, P. Amendt, J. Koch, O. Landen, H. Park, H. Robey, R. Town, A. Casner, F. Philippe, R. Betti, J. Knauer, D. Meyerhofer, C. Back, J. Kilkenny, and A. Nikroo, Plasma Phys. Controlled Fusion **52**, 124027 (2010).
[14]A. Fews and D. Henshaw, Nucl. Instrum. Methods Phys. Res. **197**, 517 (1982),
[15]R. Fleischer, P. Price, and R. Walker, *Nuclear tracks in solids: principles and applications* (University of California Press, 1975).
[16]B. Cartwright, E. Shirk, and P. Price, Nucl. Instrum. Methods **153**, 457 (1978).
[17]E. da Fonseca, T. Knöfel, and O. Tavares, M.S. thesis, Centro Basileiro de Pesquisas Fisicas (1983).
[18]H. Khan, A. Brandt, N. Khan, and K. Jamil, Nucl. Tracks Radiat. Meas. (1982) **7**, 129 (1983).
[19]J. Charvát and F. Spurnı, Int. J. Radiat. Appl. Instrum. Part D. Nucl. Tracks Radiat. Meas. **14**, 447 (1988).
[20]P. Stafford, J. Horton, K. Hogstrom, P. DeLuca Jr., and D. Holslin, Int. J. Radiat. Appl. Instrum. Part D. Nucl. Tracks Radiat. Meas. **14**, 373 (1988).
[21]R. Mishra, C. Orlando, L. Tommasino, S. Tonnarini, and R. Trevisi, Radiat. Meas. **40**, 325 (2005).
[22] Matiullah, S. Rehman, S. Rehman, and W. Zaman, Radiat. Meas. **39**, 337 (2005).
[23]K. Chan, B. Lau, D. Nikezic, A. Tse, W. Fong, and K. Yu, Nucl. Instrum. Methods Phys. Res. B **263**, 290 (2007).
[24]K. Chan, F. Ng, D. Nikezic, and K. Yu, Nucl. Instrum. Methods Phys. Res. B **263**, 284 (2007).
[25]S. Durrani and R. Bull, *Solid State Nuclear Track Detection: Principles, Methods, and Applications* (Pergamon, Elmsford, New York, 1987).
[26]R. Henke and E. Benton, Nucl. Instrum. Methods **97**, 483 (1971).
[27]D. Nikezic and K. Yu, Mater. Sci. Eng. R. **46**, 51 (2004).
[28]S. McDuffee, J. Frenje, F. Séguin, R. Leiter, M. Canavan, D. Casey, J. Rygg, C. Li, and R. Petrasso, Rev. Sci. Instrum. **79**, 043302 (2008).
[29]As the thickness of CR-39 stock can change, the CR-39 filter thickness was verified to be within 20μm of the data CR-39 thickness.
[30]J. Ziegler, J. Biersack, and U. Littmark, *SRIM - The Stopping and Range of Ions in Matter* (Pergamon, New York, 1985).
[31]D. G. Hicks, Ph.D. dissertation (Massachusetts Institute of Technology, 1999).